Journal of Molecular Structure 1261 (2022) 132887

Contents lists available at ScienceDirect

Journal of Molecular Structure

journal homepage: www.elsevier.com/locate/molstr

Review

Experimental and theoretical spectroscopic characterization, Hirshfield surface analysis, TD-DFT calculation, and nonlinear optical properties of (E)-1-[(2,4,6tribromophenyl)diazenyl]-naphthalen-2-ol azo dye

Azayez Mansour[a], Chetioui Souheyla[b,c], Megrouss Youcef[a,d], Boukabcha Nourdine[a,d,*], Djedouani Amel[e,f], Guerroudj Ahlam Roufieda[d], Meddah Araibi Noureddine[a], Chouaih Abdelkader[d]

[a] Chemistry Department, Faculty of Exact Sciences and Informatic, Hassiba Benbouali University, Chlef 02000, Algeria
[b] Environmental and Structural Molecular Chemistry Research Unit, Faculty of Exact Sciences, Department of Chemistry, University of Mentouri Brothers, Constantine 1, Constantine 25000, Algeria
[c] Faculty of Technology, University of Mohamed Boudiaf M'sila, Algeria
[d] Laboratory of Technology and Solid Properties (LTPS), Abdelhamid Ibn Badis University of Mostaganem, Mostaganem 27000, Algeria
[e] Laboratory of Analytical Physicochemistry and Crystallochemistry of Organometallic and Biomolecular Materials, University of Mentouri Brothers, Constantine 1, 25000 Constantine, Algeria
[f] Higher Normal School of Constantine, University of Constantine 3, 25000 Constantine, Algeria

ARTICLE INFO

Article history:
Received 27 January 2022
Revised 18 March 2022
Accepted 19 March 2022
Available online 20 March 2022

Keywords:
Azo dyes
UV-Vis
FT-IR
NMR
NLO
Hirshfeld surface analysis

ABSTRACT

(E)-1-[(2,4,6-Tribromophenyl) diazenyl]-naphthalen-2-ol azo dye, an organic crystal, was fully characterized by three reliable spectroscopic techniques (Fourier-transform infrared, ulltra-violet–visible, and nucleaire magnetic resonance). To support experimental results, a theoretical study has been realized to predict the best molecular structure, physico-chemical properties, and spectroscopic spectra by using the density functional theory calculations. Thus geometrical parameters, electronic transitions, vibrational frequencies, and ^{1}H and ^{13}C nuclear magnetic resonance are evaluated via comparison with experimental data. The effect of the medium dielectric constant was allowed for via self-consistent reaction field theory calculations using the polarizable continuum model with ethanol and dimethyl sulfoxide as solvents. In addition, some electric properties such as polarizability and hyperpolarizability in the static and dynamic regimes are calculated and discussed. The analysis of the obtained results of the density functional theory and time-dependent density functional theory calculations are in good agreement with the experimental data. This azo dye compound exhibits more stability and less reactivity at high polar media with a nonlinear optical aspect. In adition, Hirshfeld surface and 2D-fingerprint plots analysis shows that the H…H, O…H/H…O, C…H/H…C, N…H/H…N and Br…H /H…Br contacts are the most significant contributors.

1. Introduction

Azo dyes are synthetic compounds widely used in various fields of science and technology such as textiles, papers, leather, xerography laser materials, laser printing, materials for organic solar cells and chemosensors, *etc* [1–4]. Their production volume does not stop growing and their relative importance may even increase in the future. Azo dyes represent the most important class of dyes and constitute more than 70% of all commercial dyes [5]. Different synthetic routes have been proposed allowing obtaining the desired color properties, the yield and particle size of azo dyes. The most cited pathways are: the diazotization of an aromatic primary amine followed by coupling with one or more electron-rich nucleophiles, reduction of nitroaromatic derivatives in alkaline medium, reduction of nitroso compounds by $AlLiH_4$, and oxidation of primary amines by permanganate potassium [6–8]. The azo dyes can form covalent bonds with the textile substrates; they give permanent color highly resistant to external factors [9]. Unfortunately, its effluent released cause environmental pollution [10]. The azo dyes may be classified as mono azo, diazo,

* Corresponding author at: Chemistry Department, Faculty of Exact Sciences and Informatic, Hassiba Benbouali University, Chlef 02000, Algeria.
E-mail address: n.boukabcha@gmail.com (B. Nourdine).

https://doi.org/10.1016/j.molstruc.2022.132887
0022-2860/

or poly azo dye based on the number of azo groups present in them [11].

Heterocyclic azo dyes such as (E)−1-[(2,4,6-Tribromophenyl) diazenyl]-naphthalen-2-ol which constitutes the object of this study, have found several applications in many fields such as optical switching, molecular switches, nonlinear optical devices, etc [12–14]. They also offer other valuable properties such as their various biological activities as anti-tumor, anti-inflammatory, antibacterial, and anti-fungal agents [15,16]. Like all azo dyes, the chemical structure of E-TPDN dye is constituted by a backbone and it has an auxochrome group (OH) and a chromophoric group (N=N) bonded to the benzene ring and the naphthalene group [17,18]. The presence of halogen (brome) in benzene cycle provides improved fastness against peroxy-bleach containing wash liquors [19]. In addition, the presence of halogen as donors of electrons, which can be delocalized on the aromatic ring (s), makes it possible to increase the resonance phenomenon. This is how we can play on the color and the dyeing qualities [20].

In recent years, many experimental studies of azo dyes are supported by quantum chemical calculations [21–24]. These latter are very powerful tools to reveal the structure-performance relationship and to give information about the vibrational, electronic and structural properties of these materials with acceptable accuracy [25–28]. Several studies have been published on the synthesis and spectral properties of several azo dyes [29–31], but there is no complet report of electronic and optical properties of azo dye halogen derivatives. This is what we endeavor to show in this work through an experimental and theoretical investigations of (E)-1-[(2,4,6-Tribromophenyl) diazenyl]-naphthalen-2-ol (E-TPDN) azo dye which previously synthesized with the molecular structure solved by Chetioui et al [32]. The experiment section was carried out by using three reliable spectroscopic methods; fourier-transform infrared (FT-IR), ulltraviolet–visible (UV-Vis), and nuclear magnetic resonance (^{1}H, and ^{13}C NMR). The theoretical study is provided by means of density functional theory (DFT) and time-dependent density functional theory (TD-DFT) with traditional hybrid and long-range corrected functionals to exihibit and discus their physical, chemical, and optical properties. Hirshfeld surface analysis is performed in order to understand what kind of interatomic contacts give the largest contributions in crystal structure.

2. Experimental and computational details

2.1. Experimental details

The absorbance measurements of E-TPDN were performed with a double beam UV-Vis spectrophotometer (Specord 200) equipped with a temperature control system. The UV-Vis spectrum was recorded for wavelengths ranging from 190 to 500 nm at constant temperature T = 25 °C. The infrared spectrum was recorded on a Perkin Elmer Spectrum Two FT-IR spectrophotometer equipped with Perkin Elmer UATR-TWO diamond ATR. The ^{1}H and ^{13}C NMR spectra were recorded on a Brucker Avance III apparatus at 300 MHz and a resolution of the FID signal at 0.18 Hz/point. All solutions were prepared in chloroform-d ($CDCl_3$), and the chemical shifts (δ) are expressed in parts per million "ppm" relative to the peak of tetramethylsilane (TMS) taken as a reference.

2.2. Computational details

The ground-state calculations were performed using the Gaussian 09 package program [33] and the output files were visualized via Gauss View 5 software [34]. The ground state of the object molecule was undergone geometry optimization by DFT with B3LYP functional and 6–311++G (d, p) split valence basis set. This level of theory is commonly used to predict the properties of organic compounds and it reproduces very well the experimental geometric parameters [28,35–38]. The polarizable continuum model (PCM) [39] is included as the model of solvation by choosing chloroform as a solvent for TD-DFT, DMSO, and ethanol for DFT calculations to draw attention to solvent effects and to allow an analytical solution for the calculation of the interaction energy between the solute and continuum multipole, by comparing the results of this model with available experimental data. The theoretical infrared spectrum of the compound under investigation is calculated at B3LYP/6–311++G (d, p) by using its optimized geometries, and is visualized by the Gauss View 5.08 software and the main vibration modes have been analyzed by the VEDA program [40]. The complete assignments were performed based on the Potential Energy Distribution (PED) of the vibrational modes calculated using the VEDA4 program. The ^{1}H NMR and ^{13}C NMR chemical shifts were investigated using the standard Gauge-Independent Atomic Orbital approach (GIAO) [41,42] at B3LYP/6–311++G(d, p) level, taking tetramethylsilane (TMS) as reference. The dipole moment (μ), the mean polarizability (α), the first-order hyperpolarizability (β), and the second-order hyperpolarizability (γ) in the static and dynamic regimes were also computed to evaluate the NLO properties of E-TPDN using CAM-B3LYP/6–311++G(d, p) level of theory. These quantities are defined as [43–45]:

$$\mu = \left(\mu^2{}_x + \mu^2{}_y + \mu^2{}_z\right)^{1/2};$$

$$\alpha = 1/3(\alpha_{xx} + \alpha_{yy} + \alpha_{zz});$$

$$\beta \parallel = \left(\beta^2{}_x + \beta^2{}_y + \beta^2{}_z\right)^{1/2};$$

$$\gamma = 1/5(\gamma_{xxxx} + \gamma_{yyyy} + \gamma_{zzzz} + 2\gamma_{xxyy} + 2\gamma_{xxzz} + 2\gamma_{yyzz});$$

where $\beta_i(i = x, y, z)$ is given by $\beta i = 1/3\Sigma_{j=x,,}(\beta_{ijj} + \beta_{jij} + \beta_{jji})$.

$$\gamma = 1/15\sum_{ij}\left(\gamma_{iijj} + \gamma_{ijij} + \gamma_{ijji}\right)$$

for dc-SHG process, and

$$\gamma = 1/10\sum\nolimits_{ij}(3\gamma_{ijij} - \gamma_{iijj})$$

for dc- Kerr effect.

The molecular electrostatic potential was calculated at the same level to predict the reactive sites for the electrophilic or nucleophilic attack for the considered compound. Finally, the Hirshfeld surface analysis was performed using Crystal Explorer 17.5 program [46].

3. Results and discussion

3.1. Molecular geometry

The structure of the E-TPDN molecule has been optimized by using the DFT method and the B3LYP/6–311++G(d, p) level, which is compared experimentally by Chetioui et al [32]. (Fig. 1). It is noted that this system has negative energy and no imaginary frequency are obtained from the frequencies calculation, which indicates that this structure corresponds to a stationary state. We report in Table 1, the calculated geometrics parameters (bond lengths and angles) and those obtained experimentally.

The global image of these results shows that B3LYP/6-311++G(d,p) is better at predicting with acceptable accuracy geometric parameters from X-ray diffraction. For example, the calculated C–C within rings, C-Br, C–O, and N=N bonds lengths values are in the ranges 1.367–1.446, 1.911–1.913, 1.331, and 1.27 Å, agree

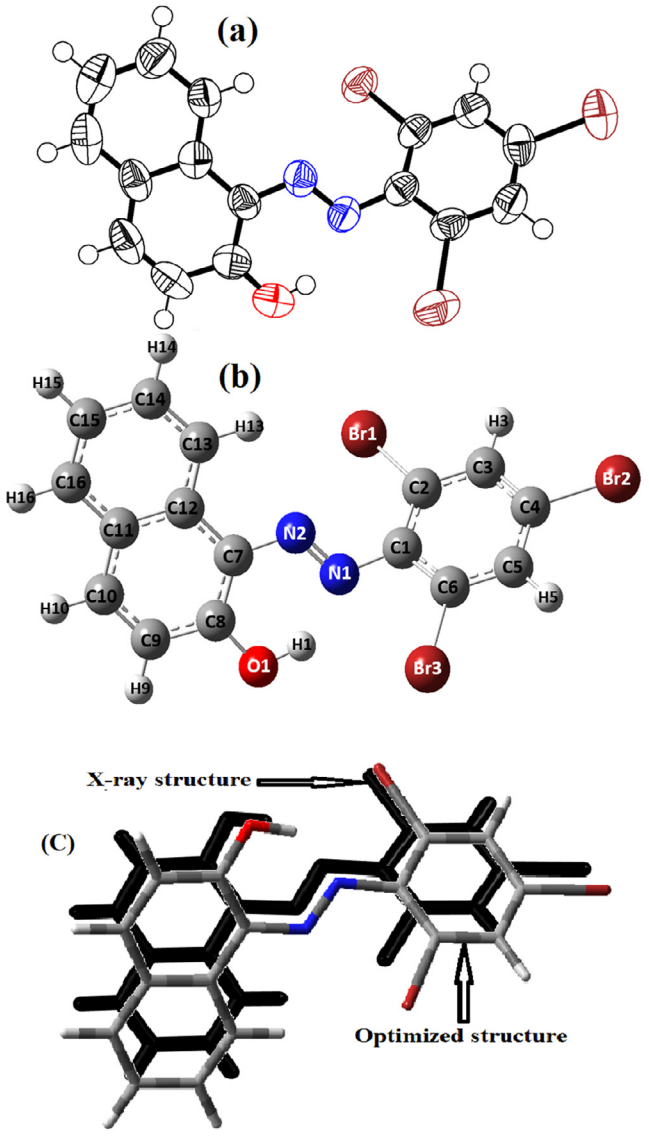

Fig. 1. (*a*) Experimental structure and (*b*) optimized structure of E-TPDN ***(c)***The superimposition of the experimental and optimized structure.

with the correspondent experimental values ranging of 1.35–1.455 and 1.887–1.892, 1.311 and 1.292 Å, respectively. Whereas, the maximum deviations of valence angles and tetrahedral angles values from theoretical and experimental data do not exceed 2.87 and 2.3°, respectively except for N2- N1-C1-C2 which is equal to 12.7° We note that this structure is not planar as indicated by tetrahedral angles N2-N2-C1-C2 (−38.6°) and N1-N2-C7-C12 (−178.4°). In addition, low root mean square deviations (RMSD) values show the excellent correlation between the calculated and experimental geometric parameters.

3.2. Hirshfeld surface analyses and two-dimensional fingerprint plots

3.2.1. Hirshfeld surface analyses

Analysis of calculated Hirshfeld surfaces has become an invaluable technique for crystallographers and crystal engineers, as it provides additional information on the weak inter and intramolecular interactions that influence the packing of molecules in crystals [47–49]. Hirshfeld surfaces can be mapped with different properties namely; electrostatic potential, d_{norm}, shape-index, and curvedness [50]. The function d_{norm} (normalized contact), i.e. the sum of

Table 1
The experimental and calculated geometric parameters of E-TPDN.

			X-ray	B3LYP/6-311++G(d, p)	
Bond lengths (Å)					RMSD bonds lengths(Å)
Br1	C2		1.887	1.913	0.014
Br2	C4		1.889	1.911	
Br3	C6		1.892	1.912	
O1	C8		1.311	1.331	
N1	N2		1.292	1.270	
N1	C1		1.414	1.413	
N2	C7		1.369	1.379	
C1	C2		1.387	1. 407	
C1	C6		1.406	1.406	
C2	C3		1.389	1.392	
C3	C4		1.378	1.389	
C4	C5		1.377	1.389	
C5	C6		1.373	1.388	
C7	C8		1.409	1.413	
C7	C12		1.455	1.446	
C8	C9		1.420	1.416	
C9	C10		1.350	1.367	
C10	C11		1.420	1.424	
C11	C12		1.418	1.425	
C11	C16		1.408	1.415	
C12	C13		1.400	1.413	
C13	C14		1.369	1.379	
C14	C15		1.390	1.409	
C15	C16		1.351	1.376	
Bond angles (°)					RMSD angles (°)
Br2	C4	C3	119.9	119.36	1.134
C1	C2	C3	122.5	121.54	
Br1	C2	C1	120.4	122.05	
C4	C5	C6	120.2	118.42	
Br3	C6	C1	122.5	119.63	
Br3	C6	C5	116.4	117.81	
C1	C6	C5	121.0	122.53	
N2	C7	C8	125.2	123.92	
N2	C7	C12	114.8	116.37	
C8	C7	C12	120.0	119.70	
O1	C8	C7	122.5	122.50	
C7	C8	C9	119.3	120.07	
C8	C9	C12	120.3	120.32	
C9	C10	C11	123.2	121.97	
C10	C11	C16	122.5	121.46	
C12	C11	C16	119.4	119.59	
C7	C12	C11	119.0	118.98	
C13	C14	C15	120.9	120.95	
C14	C15	C16	120.0	119.62	
C11	C16	C15	120.9	120.73	
N2	N1	C1	115.0	115.48	
N1	N2	C7	116.3	117.47	
N1	C1	C6	117.7	118.13	
C2	C1	C6	117.0	116.92	
Dihedral angles (°)					RMSD angles (°)
N2	N1	C1	C2 -38.6	-51.3	0.99
N1	N2	C7	C12 -178.4	-178.5	
N2	C7	C8	O1 -3.0	-0.91	
C2	C1	C6	C5 -3.2	-1.92	
C2	C3	C4	C5 -0.8	-0.87	
C7	C8	C9	C10 1.3	-0.60	
C9	C10	C11	C12 1.0	0.23	
C13	C14	C15	C16 -0.9	-0.03	
C12	C11	C16	C15 0.2	0.03	

the interior and exterior distances, both normalized by the van der Waals radius (r^{vdW}) of the corresponding atom inside and outside the Hirshfeld surface it is defined by:

$$d_{\text{norm}} = \frac{d_i - r_i^{\text{vdw}}}{r_i^{\text{vdw}}} + \frac{d_e - r_e^{\text{vdw}}}{r_e^{\text{vdw}}}$$

(*di*): Interior distance, i.e. the distance from the Hirshfeld surface to the nearest atom inside the surface, (*de*): Exterior distance, i.e. the distance from the Hirshfeld surface to the nearest atom

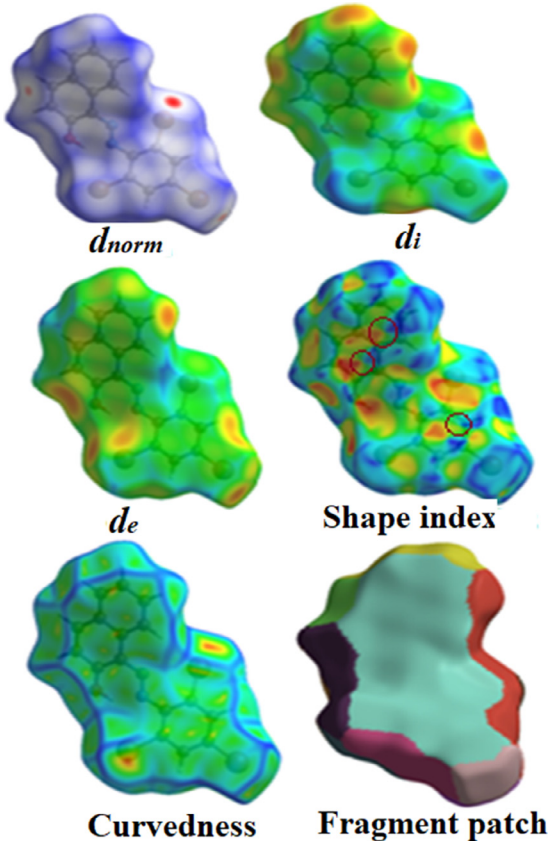

Fig. 2. Hirshfeld surface analysis of the E-TPDN compound with d_i, d_e, d_{norm}, shape index, curvedness and fragment patch.

outside the surface [51]. Using the privacy of colors for illustration, the function d_{norm} displays a surface with a blue-white-red-colored scheme, in which the red and blue-colored indicate the shorter and longer intermolecular contacts, respectively, while the white color represents the contacts around the van der Waals radii [52] Fig. 2. shows the Hirshfeld surface distribution of the organic compound (E-TPDN) by d_{norm}, d_i, d_e, shape index, curvedness and fragment patch mapping obtained using the Crystal Explorer 17.5 program by inputing the crystallographic information file (CIF) data.

We can visualize the intermolecular interactions donors and acceptors via the blue and red regions around the participant atoms that correspond to the positive and negative electrostatic potential on the surface, respectively. It is also well established from the Hirshfeld surfaces of the molecules being connected to each other by stacking interactions which can be observed in the neighboring red and blue triangles (highlighted in red) in the surface of the shape index (Fig. 2). The following blue triangles are convex regions derived from the existence the carbon atoms of the aromatic ring inside the surface, whereas those of the red triangles are concave areas. According to the mapping of shape index and curvedness it is easy to explore the existence a possible stacking of $\pi-\pi$ bonds of aromatic rings [53]. Furthermore, it is clearly seen in Fig. 3 that the red region represents the intermolecular interactions Br…Br and Br…H in the crystal packing. The reciprocal contacts Br2…H10/H10…Br2, displayed on the HS mapped on d_{norm} as small light red spots, are the neighborhood of 3.24 Å. The hydrogen bonds contribute strongly to the stabilization of the crystal packing of the investigated molecule through molecular interactions. The three-dimensional Hirshfeld surface views of E-TPDN crystal compound on d_{norm} are plotted in Fig. 3 and run from −0.104 to 1.198 Å. The red areas are the closest contacts and the nearest negative areas, while the blue areas are those with longer contacts and a positive d_{norm} of contact. The regions colored white represent weaker contacts with contact distances approximately at the vdW distance ($d_{norm} \approx 0$).

3.2.2. Two-dimensional fingerprint plots

Fingerprint plots are important for the ability to identify interatomic connections and structure information of molecules [54]. Based on the two-dimensional fingerprint plots, intermolecular interaction behavior of the compound E-TPDN has been quantitatively investigated. In this part, there are complementary zones apparent, in which a molecule acts as a donor ($d_e > d_i$) while the other acts as an acceptor when $d_e < d_i$ Fig. 4. illustrates the fingerprint traces for all contributions to the surface. In particular, the fringprint plots contain mutual contacts H…X/X…H at which the X atom is positioned on the interior or exterior of the resulting Hirshfeld surface acting as H atom acceptor. As illustrated in Fig. 4, H…Br/Br…H interactions represent the largest percentage with 29% of all contacts shown in the fingerprint plot. The contacts H…H are located in the center of the dispersed points. The H…H contacts correspond to 21.2% of the total Hirshfeld surface at about $d_i = d_e \sim 1.2$ Å. The C...H/H...C contacts occupied 13.3% in terms the total area value being the third significant element of the crystal packing. Whereas the C...C and O...H/H...O have a minimal participation of 11.5% and 6.1%, respectively. The three contributing fires among the interacting atoms on the total HS surface are the Br…Br, Br…C/C…Br and N…C/C…N contacts, thus covering 6.9%, 5% and 2.9% of the global surface, respectively.

3.3. Uv-Vis analysis

The identification of the nature of different electronic transitions is based on the analysis of the molecular orbital localization and their coefficients. Our theoretical calculations allowed us to detect absorption wavelengths corresponding to electronic transitions calculated from the ground state. Thus, three peaks centered at absorption wavelengths 231, 309, and 446 nm are observed experimentally (Fig. 5), attributed to the electronic transitions related to the lone pair of the nitrogen, the N=N function conjugated to the rings chromophore of phenyl and naphthyl groups. These electronic transitions are comparable with those calculated using the theoretical level TD-DFT/B3LYP/6–311++G (d, p) and which are equal to 273.98, 332.38, and 428.33 nm. The calculated energies of the excited states, the strength of the oscillator, the electronic transitions, and their percentage contributions to the wave function of the excited state are collated in Table 2. According to the theoretical UV-Vis spectrum of the studied molecule, the electronic absorption band calculated at 428.33 nm is attributed to the combination of two main electronic transitions; HOMO/LUMO with 65.72% and HOMO-1/LUMO with 27.43% witch correspond to $\pi \rightarrow \pi^*$ electronic transition partially overlapping with the $\pi \rightarrow \pi^*$ of the azo bond absorption band. The band calculated 332.38 nm is attributed to HOMO-4/LUMO (84.3%) with a slight contribution from the transition HOMO-1/LUMO (7.56%). The third band, which is centered on the 273.98 nm wavelength corresponds to $n \rightarrow \pi^*$ electronic transition, is a combination of five electronic transitions, of which the HOMO-6/LUMO (29.26%) and HOMO-1/LUMO+2 (28.36%) contributions are the most important. The absorption bands attributed to $\pi \rightarrow \pi^*$ and $n \rightarrow \pi^*$ electronic transitions suggest that an intramolecular charge transfer takes place within this molecule. The strength of the oscillation is a characteristic of the intensity of the bands and the more the electronic transition energy is lower, the more the transition is allowed. Thus, the transition centered on wavelength 428.33 is the most permitted because it is characterized by the low transition energy with an oscillator strength of 0.325. It should be noted that

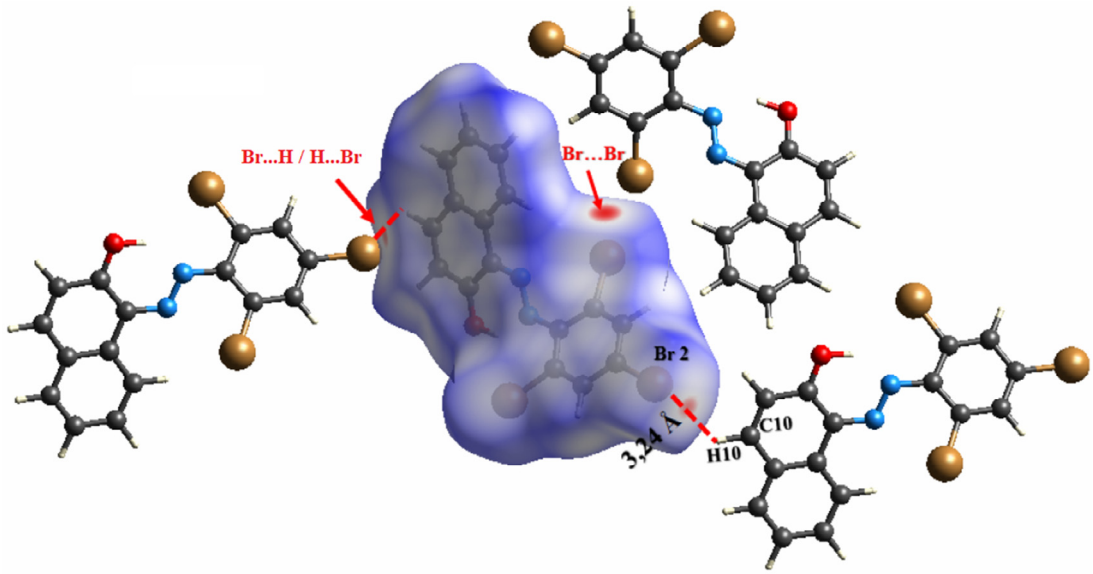

Fig. 3. The view of the three-dimensional Hirshfeld surface of E-TPDN plotted over d_{norm}.

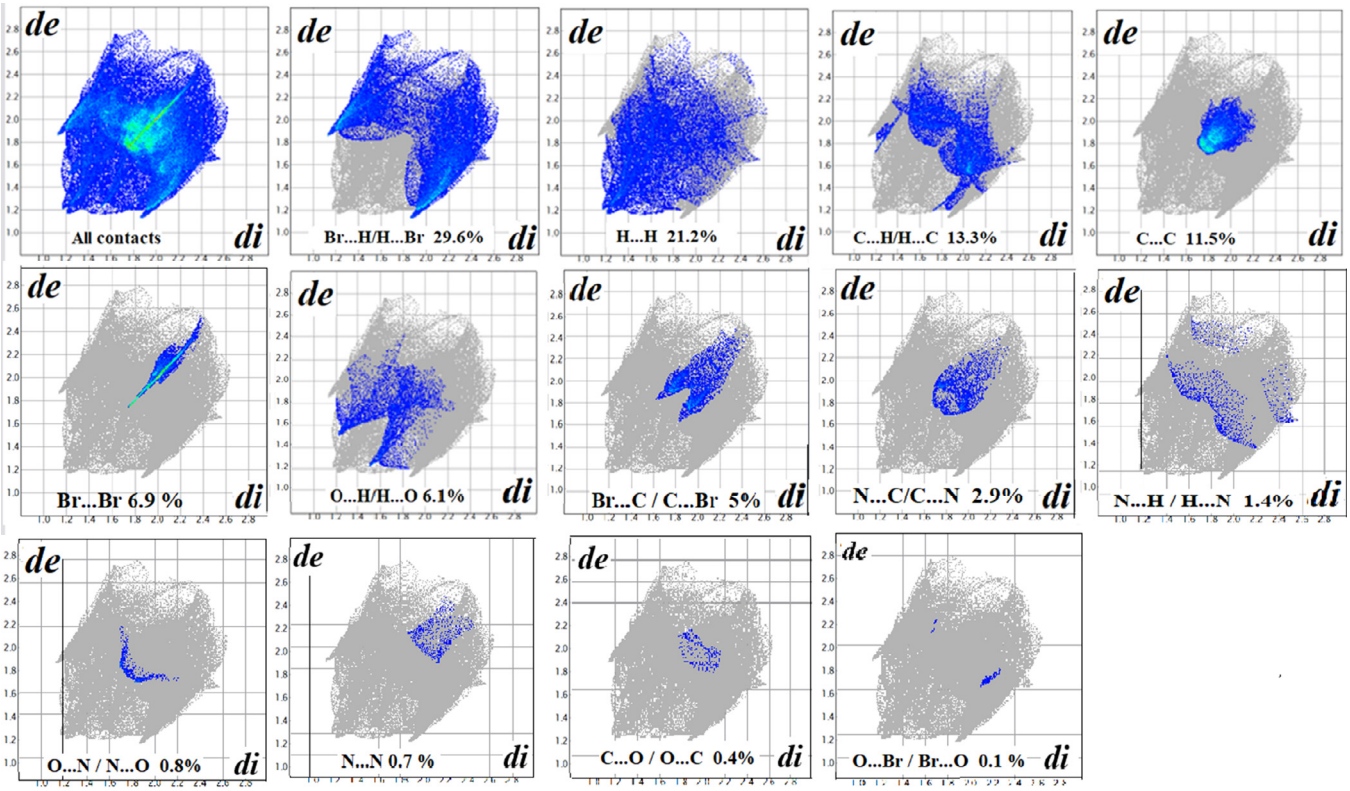

Fig. 4. The 2D- Fingerprint plots showing the overall contribution to the total HS area and the individual percentages of the diverse intermolecular contacts of E-TPDN molecule.

the electronic transition observed in the visible range corresponds to a broadband, which can be explained by the contribution of two electronic transitions (428.33 and 478.91 nm).

3.4. Frontier molecular orbitals and global chemical reactivity descriptors analysis

The distributions and energy level of frontier molecular orbitals (HOMO and LUMO) of E-TPDN shown in Fig. 6 indicate that the HOMO is located over the π system of the phenyl and naphthyl rings, the lone pair of brome atoms and the azo group, while the LUMO is located over the π^* system of two rings 2, 3 and π^* of the azo group. The energy gap between the HOMOs and LUMOs represents the critical parameter in determining the molecular electrical transport properties which help the electron conductivity measurement. The frontier molecular orbitals' energies (HOMO, LUMO) were used to calculate the global chemical reactivity descriptors of the molecule, such as the ionization potential (IP), the electron affinity (A), the electronegativity (χ), the global chemical hardness (η), the global chemical softness (S), the chem-

Table 2
Electronic transitions, oscillator strength and major contributions for E-TPDN.

Experimental	B3LYP/6-311++G(d, p)				
λ (nm)	λ(nm)	E (eV)	Osc. Strength	Major contributions	
				HOMO-6/LUMO	(29.26%)
				HOMO-1/LUMO+2	(28.36%)
231	268.74	4.6135	0.0536	HOMO/LUMO+5	(7.83%)
				HOMO-5/LUMO	(10.68%)
				HOMO/LUMO+4	(14.62%)
309	329.91	3.7581	0.1127	HOMO-4/LUMO	(84.3%)
				HOMO-1/LUMO	(7.56%)
446	428.33	2.9114	0.3252	HOMO-1/LUMO	(27.43%)
				HOMO/LUMO	(65.72%)

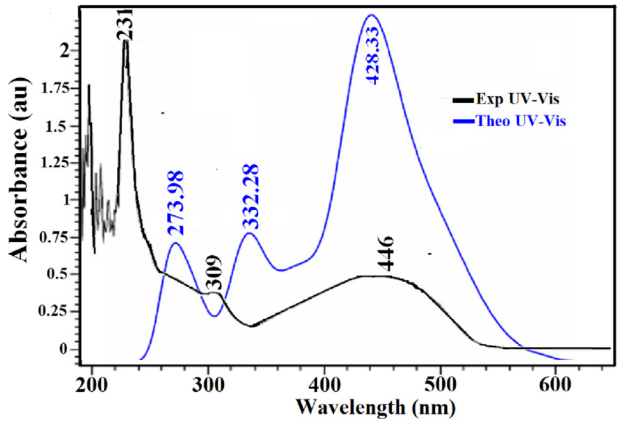

Fig. 5. A comparison of experimental and theoretical UV–Vis spectra of E-TPDN.

Table 3
Global reactivity parameters of E-TPDN.

	DFT/B3LYP/6–311++G(d,p)		
Parameters (eV)	In vacuum ($\varepsilon = 1$)	In ethanol ($\varepsilon = 24.85$)	In DMSO ($\varepsilon = 46.82$)
HOMO	−6.246	−6.285	−6.291
LUMO	−2.984	−3.004	−3.009
$\Delta E = E_{LUMO} - E_{HOMO}$	3.262	3.281	3.282
IP = -HOMO	6.246	6.285	6.291
A = -LUMO	2.984	3.004	3.009
$\chi = -\frac{1}{2}(E_{LUMO} + E_{HOMO})$	4.165	4.644	4.650
$\eta = \frac{1}{2}(E_{LUMO} - E_{HOMO})$	1.631	1.640	1.641
$S = 1/2\eta$ $(eV)^{-1}$	0.3065	0.3048	0.3047
$\mu = \frac{1}{2}(E_{LUMO} + E_{HOMO})$	−4.165	−4.644	−4.650
$\omega = \mu^2/2\eta$	5.317	6.573	6.588

ical potential (μ) and the electrophilicity index (ω) [55]. This last parameter is also a possible descriptor of the biological activity of molecules [56]. These descriptors are expressed as follows [57–64], and their values obtained in different media are ported in Table 3.

As it is well known, a high-value energy gap (ΔE) indicates that the molecular structure has higher kinetic stability, and a lower chemical reactivity [65]. For this compound, as the solvent dielectric constant increases, the value of ΔE has increased, the structure exhibits then more stability and less reactivity. Ionization potential, affinity, and electronegativity values have increased with increasing solvent polarity; therefore, a high polar environment decreases the electron donor character and augments the electron acceptor character for E-TPDN. The global chemical hardness values have increased and the global softness values have decreased slowly, with the increasing solvent polarity; E-TPDN exhibits less reactive properties in the high polar media with a high probability of intramolecular charge transfer at the media with a lower dielectric constant. The electrophilicity index values have increased while the chemical potential values have decreased with increasing solvent polarity; these values suggest that this compound has exhibited a good electrophile character in the DMSO medium.

3.5. Vibrational band assignments

The infrared (IR) spectrum of this compound was recorded in the range of 4000–400 cm^{-1}. Both theoretical and experimental IR spectra of E-TPDN are shown in Fig. 7. This compound consists of 31 atoms, which undergo 87 normal modes of vibrations with no imaginary frequency was detected using the level B3LYP with 6–311++G (d, p) basis set. Fundamental vibrational modes calculated and experimental corresponding data are given in Table 4. For this method, the calculated vibrational frequencies are scaled by a factor of 0.9614.

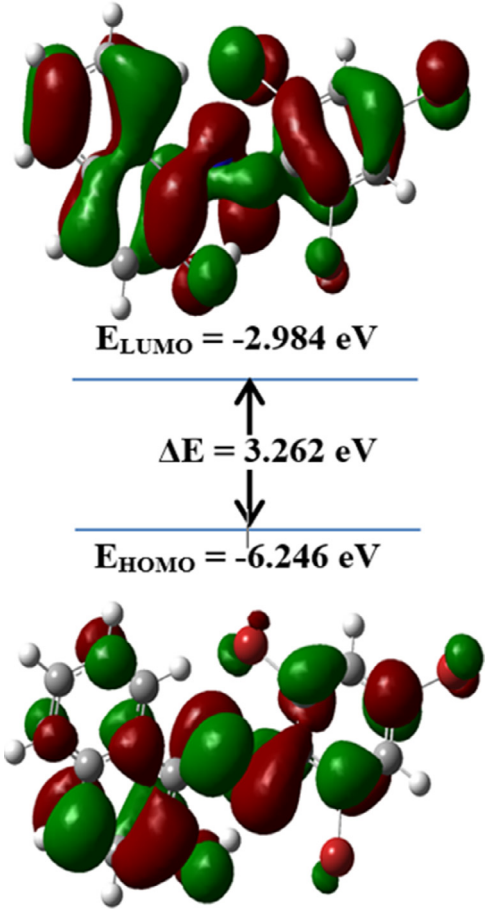

Fig. 6. Frontier molecular orbitals of E-TPDN.

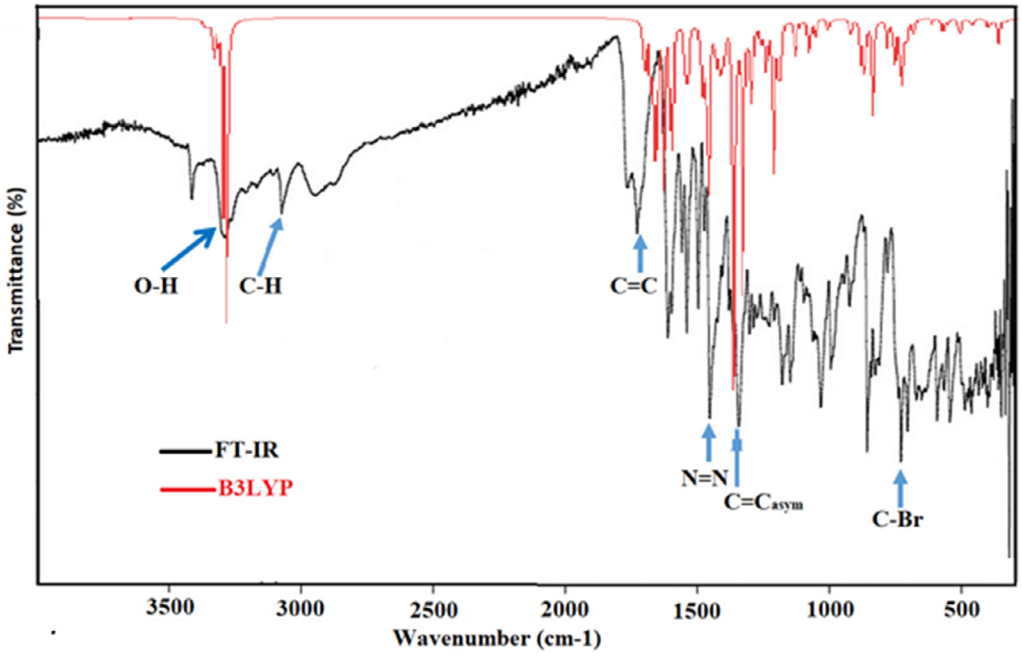

Fig. 7. Experimental and theoretical IR spectra of E-TPDN.

Table 4
Experimental and calculated vibrational frequencies and assignments with PED of E-TPDN.

FT-IR (cm^{-1})	B3LYP/6–311++G(d,p)	Assignments with PED>10%
	Scaled freq (cm^{-1})	
3286	3024	ν OH (97%)
3208	3095	ν CH (98%) ring 1
	3089	ν CH (95%) ring 3
	3074	ν CH (92%) ring 2
	3065	ν CH (83%)$_{sym}$ ring 3 + ν CH (10%) $_{asym}$ ring3
3072	3049	ν CH (83%) ring 3
2999	3039	ν CH$_{asym}$ (10%) ring 3 + ν CH$_{asym}$ (78%) ring2
1598	1592	ν CC$_{asym}$(60%) ring 2, ring 3
	1570	[ν CC (50%) + δ HCC (14%)] ring 2, ring 3
1559	1555	δ HOC (19%) + δ CCC$_{asym}$ (11%)
1540	1528	δ HCC (15%) + ν CC$_{asym}$ (61%) ring 2,ring3
1497	1498	ν CC (18%) + ν CC$_{asym}$ (23%) + ν CC(18%) + ν CC$_{asym}$ (50%) + ν CC$_{asym}$ (13%) + δHCC (11%)
1454	1453	δ HCC (19%) + ν NN (24%)
	1442	δ HOC (26%) + δ HCC (10%) ring 2, ring3
	1399	δ HCC (30%) + ν NN (23%)
	1392	δ HCC (15%) + δ CCC (15%) + δ HOC (10%) + ν CC (15%)
1364	1375	δ HCC (30%) + δ CCC (13%)+ ν CC$_{asym}$ (12%) + ν NC$_{sym}$ (12%)
1344	1338	[ν CC (38%) + δ HCC (36%)] ring 1
	1323	ν CC$_{asym}$(50%)
1303	1287	δ HCC (15%) + δ CCC (13%) +ν CC (10%) + ν NC (11%)
1248	1236	ν CC$_{asym}$ (79%) ring 1
1210	1190	δ HCC (26%) + ν CC (22%) + ν NC (13%)
1053	1032	δ CCC (15%) + δ CCC$_{asym}$ (48%) + ν BrC (11%)
996	964	δ CCC$_{asym}$(12%) + τ HCCC (70%) + ν CC (17%) + ν CC$_{asym}$ (10%)
	948	τ CCCC$_{asym}$ (14%) + τ HCCC (63%)
	893	δ CCC$_{asym}$ (11%) + δ NNC (17%)
858	857	τ HCCC (88%)
828	810	τ HCCC (58%)
	764	δ CCC (19%) + ν BrC (12%)
739	755	τ CCNN (12%) + Out τ HCCC (41%)
706	710	δ CCC (42%) + ν BrC$_{asym}$ (32%)
	696	τ CCCC$_{asym}$ (27%)
672	670	τ HCCC$_{asym}$ (11%) + τ CCCC(44%)
546	557	τ HCCC (11%) + τ HCCC (42%)
489	484	τ CCCC (84%) ring 1
403	403	τ CCCC$_{asym}$ (17%) + δ CCO (30%) + δ BrCC$_{asym}$ (12%)

ν: stretching; *sym*: symmetric; *asym*: asymmetric; δ: bending; τ: twisting. Vibrational modes are based on the potential energy distribution (PED) and only contributions over 10% are given. ring 1: C1C2C3C4C5C6; ring 2: C7C8C9C10C11C12; ring 3: C11C12C13C14C151C16.

Table 5
The experimental and calculated ^{1}H and ^{13}C NMR chemical shifts of E-TPDN.

	Chemical shifts (ppm)			
	Experimental	B3LYP/ 6–311G++(d, p)	Mean absolute errors (MAE)	Correlation factors (R^2)
^{1}H NMR			0.345	0.92
H3	7.52	7.85		
H5	7.52	7.85		
H9	6.95	7.42		
H10	7.68	8.30		
H13	8.64	9.14		
H14	7.62	7.87		
H15	7.46	7.72		
H16	7.83	8.04		
^{13}C NMR			5.04	0.83
C1	153.50	155.84		
C2	123.56	136.46		
C3	133.82	136.19		
C4	126.24	139.11		
C5	133.82	136.19		
C6	123.56	136.46		
C7	140.80	141.24		
C8	168.19	161.55		
C9	122.23	126.99		
C10	130.98	134.83		
C11	128.31	133.08		
C12	133.42	139.91		
C13	127.78	129.40		
C14	129.84	131.55		
C15	128.67	132.25		
C16	129.43	130.53		

Some fundamental peaks of E-TPDN are shown in the experimental FT-IR and theoretical IR spectra as discussed in this study.

The C–H stretching vibrations of aromatics rings appear in the range of 3100–3000 cm^{-1} and the experimental data indicate that this mode is observed in the region of 3208–3000 cm^{-1}. The C–C bands of aromatic rings appear in the regions 1592–1570, 1528–1498 and at 1323, 1236, 1190, 964 cm^{-1}. The corresponding modes of experimental IR spectra are observed at 1598.45, 1559–1540, and 1497 cm^{-1}. The experimental wave number (1454 cm^{-1}), attributed to the azo (N=N) band is better predicted by the theoretical model of calculation (1453 cm^{-1}). The OH band of the experimental infrared spectrum and the theoretical value of this band appear at 3286 and 3024 cm^{-1}, respectively. We note here that the theoretical value of OH stretching is underestimated because the presence of a hydrogen bond (OH….N1) reduces the degree of freedom of the O-H bond which reduces its frequency of vibration. The C-Br stretching vibrations appear at 764–710 cm^{-1} and CN stretching vibrations appear at 1375, 1287, 1190 cm^{-1}. All bending vibrations occur in plan in the region 1600–400 cm^{-1} and are accompanied by either elongation and/or twists. The corresponding vibration frequencies are then considered as soft modes. The torsion modes appear in the range from 1000 to 400 cm^{-1}, some of which are out of plane such as the mode τ HCCC observed at 755 cm^{-1}.

3.6. NMR spectra analysis

As shown in Fig. 1, this molecule comports 8 aromatic protons and one proton of a hydroxyl group. The correctness of the assignment was verified from the multiplicity of the signals. Experimental and theoretical values of chemicals shifts of the E-TPDN are listed in Table 5. The analysis of both ^{1}H NMR spectra showed the majority of signals in the aromatic region which corresponds to the aromatic structure of this species. Thus, the signals characteristic of the aromatic protons appear between 6.95 and 8.64 ppm. Chemical shifts obtained by B3LYP/6–311++G (d, p) are also in the aromatic region (Fig. 8), and the maximum deviations of values of chemical shifts do not exceed 0.5 ppm. The experimental ^{13}C NMR chemical shifts values are ranging from 122.23 to 168.19 ppm, whereas those computed from the B3LYP/6–311++G(d,p) level are found to be in the range 126.99 to 161.55 ppm. Therefore, the overall computed and measured ^{1}H and ^{13}C NMR chemical shift of this azo dye are in agreement as can be seen in Table 5. Thus B3LYP/ 6–311++G (d, p) is considered as a good level of calculation for predicting the values of chemical shifts of this type of compound.

3.7. Nonlinear optical properties

The NLO properties of the organic molecules arise from delocalized π electrons moving along the molecule. The increase of the conjugation on molecule leads to an increase of the polarizability and the mean first-order hyperpolarizability of organic molecules increase [66]. The E-TPDN molecule is formed from a conjugated π system, resulting in intramolecular charge transfer and high hyperpolarizability that promote the ONL response.

To investigate the NLO behavior of E-TPDN, the electric dipole moment, static and dynamic (frequency-dependent) polarizability, first and second-order hyperpolarizabilities were evaluated using the CAM-B3LYP/6–311++G(d, p) in the gas phase and compared at those of unsubstituted form of this dye. CAM-B3LYP functional can be considered as a suitable choice especially for the prediction of the electronic hyperpolarizabilities of organic molecules [67–70]. These properties can be calculated using (μ_x, μ_y, μ_z), (α_{xx}, α_{yy}, α_{zz}), (β_{xxx}, β_{xyy}, β_{xzz}, β_{yyy}, β_{yzz}, β_{xxy}, β_{zzz}, β_{xxz}, β_{yyz}), and (γ_{xxxx}, γ_{yyyy}, γ_{zzzz}, γ_{xxyy}, γ_{xxzz}, γ_{yyzz}) tensors components.

The dynamic hyperpolarizabilities were also evaluated since observed data are nearly always obtained at incident optical fields. These properties are calculated at 1064 nm ($\hbar\omega$ = 0.04282 a.u.) to minimize resonance enhancements. We then presented the quantities $\beta_{||z}$ (-2ω; ω, ω) for the nonlinear optical Second Harmonic Generation (SHG), $\beta_{||z}$ ($-\omega$; ω, 0) for electro-optical pockels effect (EOPE), $\gamma(-\omega;\omega,0,0)$ for the quadratic electro-optical (dc-Kerr effect), and $\gamma(-2\omega;\omega,\omega,0)$ for (dc-SHG). We note that the dispersion effects or dynamic polarizability α ($-\omega$, ω) is also evaluated at the

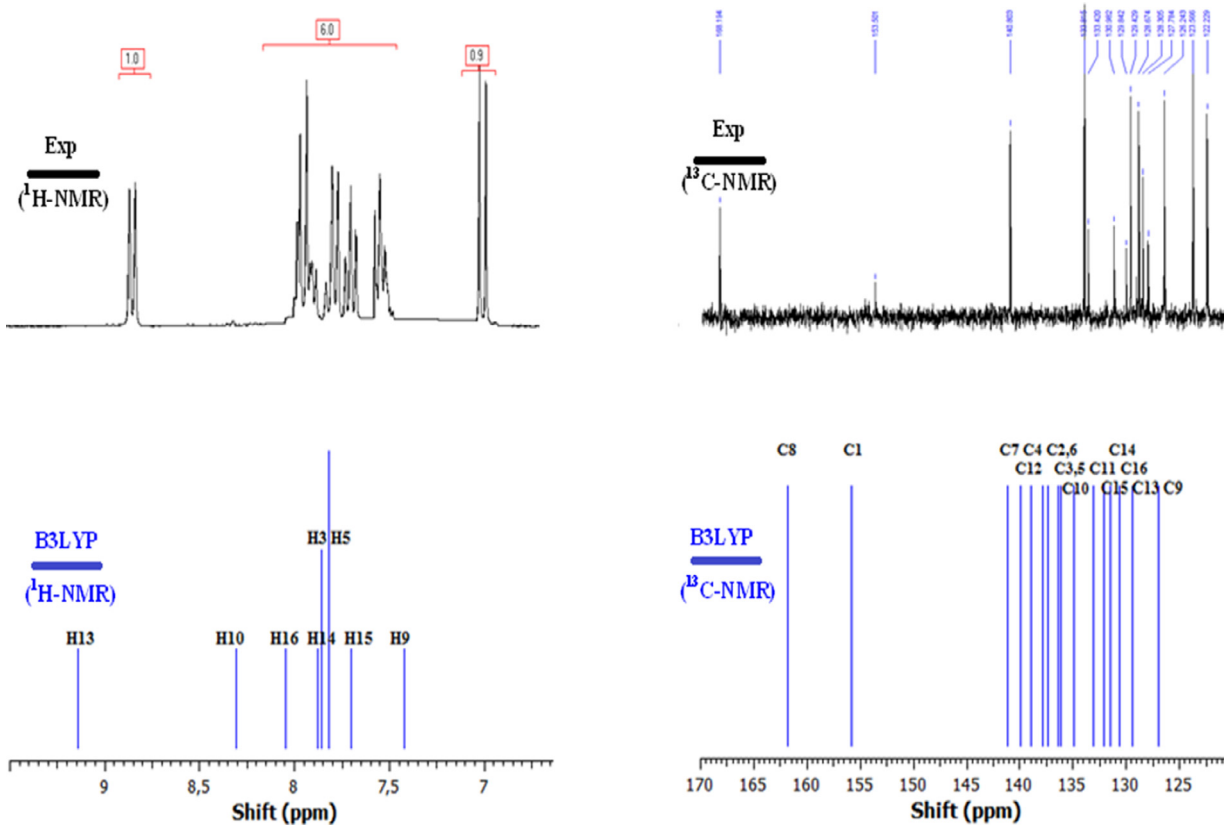

Fig. 8. Experimental and theoretical (a) ^{1}H NMR and (b) ^{13}C NMR spectra of E-TPDN.

$\hbar\omega = 0.04282$ a.u. The values of these electric properties are reported in the Table 6.

3.7.1. Dipole moment, and static and dynamic polarizabilities of E-TPDN

As can be seen in Table 6, the title compound has a non-zero dipole moment value. This magnitude indicates that this molecule may be entering intermolecular interactions involving non-bonded type dipole-dipole interactions. The values of the dipole moment obtained from CAM-B3LYP/6–311++G(d, p) in the gas phase is equal to 1.9848 D, where the highest value of the dipole moment is observed for the μ_x component. The polarization of the molecule becomes more important if the molecule is less symmetrical. The value of this property is found to be 44.1243 $\times$ 10^{-24} esu and α_{xx} is the largest component among the polarizability, this indicates that the variation of this component following x-direction is important. This molecule is considered as a soft species because it corresponds to a high value of polarizability compared to that obtained for the unsubstituted form of this dye and which is equal to 35.432 $\times$ 10^{-24} esu. The frequency-dependent polarizability evaluated at $\hbar\omega = 0.04282$ a.u. is slightly significant, increasing the static polarizability value by 1.4064 $\times$ 10^{-24} esu.

3.7.2. Static and dynamic hyperpolarizabilities of E-TPDN

Nonlinear optics strongly depends on the symmetry of the medium. Centrosymmetric medium is not active in quadratic nonlinear optics, because, in the presence of an inversion center, the first hyperpolarizability (β) is canceled. For the compound under investigation, the static first hyperpolarizability value is equal to 0.275 $\times$ 10^{-30} esu. This low value can be explained by the weak donor-acceptor character of the groups constituting this compound, or even the charge transfer is relatively low. Furthermore, the short length of the bridge between electron donor and acceptor groups may reduce the nonlinear optical properties of the E-TPDN molecule. We note that the dispersion effects enhance the static (0;0,0) values by 0.29 $\times$ 10^{-30} and 1.58 $\times$ 10^{-30} esu for the EOPE and SHG processes, respectively.

The second-order hyperpolarizability (γ) value depends on the extent of electron conjugation and the nature of substituents. In the title compound, the presence of the Br group attached to the benzene ring contributes to the augmentation of the conjugation and delocalization of electrons within the molecule. This electron delocalization induces a nonlinear behavior in this molecule. In addition, the dipole moment of E-TPDN, which is not large enough, favors obtaining significant values of second-order hyperpolarizabilities [71]. The computed value of γ for the static regime of the E-TPDN molecule is 80.245 $\times$ 10^{-36} esu, this value is significant compared to that obtained for the unsubstituted form of this molecule which has the value of 61.0023 $\times$ 10^{-36} esu. As should be expected γ $(-2\omega,\omega,\omega,0) > \gamma(-\omega,\omega,0,0)$, the dispersion effects enhance thus the static $\gamma(0;0,0;0)$ value by 23.5% and 131.7%, for the dc- Kerr effect and dc-SHG process, respectively. The statics polarizability and first order hyperpolarizability values obtained for E-TPDN are found almost similar to those of Sudan Red G which is worth (40.68 $\times$ 10^{-24} esu and 3.95 $\times$ 10^{-30} esu), respectively [72].

3.8. Molecular electrostatic potential

An analysis of the molecular electrostatic potential surface (MEPS) has been affected to validate the evidence about the reactivity of the compound under investigation. This analysis allows predicting the reactive nucleophilic and electrophilic sites of the studied molecule [73]. The MEPS can be therefore providing information on the sign of different molecular regions of E-TPDN, as it was a useful tool in the prediction of the susceptibility of the studied compounds towards electrophiles and nucleophiles. Colors

Table 6
Electric dipole moment (μ), static linear polarizability (α), static first-order hyper polarizability (β) and static second-order hyper polarizability (γ) values of E-TPDN.

NLO parameters	CAM-B3LYP/6–311++*G*(d, p)		
Dipole moment			
μ_x	−1.767		
μ_y	−0.6844		
μ_z	−0.5905		
μ (D)	**1.9848**		
Polarizability	α (0,0)	α (-ω, ω)	
α_{xx}	440.642	461.974	
α_{yy}	272.579	277.289	
α_{zz}	180.074	182.506	
α (au)	**297.765**	**307.256**	
α *10^{-24} (esu)	**44.1243**	**45.5307**	
First-order hyperpolarizability	***β*(0,0,0)**	**β (-ω,ω,0)**	**β (−2ω, ω,0)**
β_{xxx}	1083.49	1420.12	2775.83
β_{yxy}	−55.5932	−66.2437	−43.2713
β_{zzx}	−80.0911	−81.4289	−52.9563
β_{yyy}	−97.999	−99.5315	−89.0314
β_{zzy}	9.3745	12.2598	28.5397
β_{yxx}	92.8809	132.21	159.26
β_{zzz}	−35.4519	−36.4822	−31.5
β_{zxx}	53.9523	93.4547	170.512
β_{yyz}	34.5571	40.3841	59.4087
β (au)	**31.8345**	**65.4926**	**214.832**
β *10^{-30} (esu)	**0.275**	**0.5658**	**1.8559**
Second-order hyperpolarizability	***(0,0,0,0)***	**γ (-ω, ω,0,0)**	**γ (−2ω,ω, ω,0)**
γ_{xxxx}	546,687	705,821	1,481,110
γ_{yyyy}	63,404.1	68,353.3	78,937.8
γ_{zzzz}	39,846.9	42,844.8	48,702.4
γ_{xxyy}	33,217.5	41,234.8	58,691.6
γ_{xxzz}	22,687	27,886.6	35,623.1
γ_{yyzz}	17,425.9	18,933.9	21,908.8
γ_{yxyx}	-	37,655.5	71,499.1
γ_{zxzx}	-	25,528.9	46,480.4
γ_{zyzy}	-	18,836.8	22,248.4
γ_{zyyz}	-	–	21,874.9
γ_{zxxz}	-	–	29,418.7
γ_{yxxy}	-	–	44,607.9
γ (au)	**159,321**	**196,797**	**369,167**
γ *10^{-36} (esu)	**80.245**	**99.1209**	**185.938**

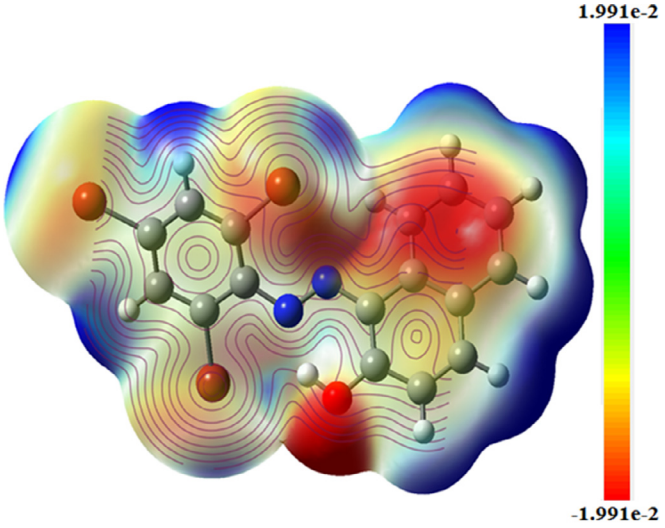

Fig. 9. Molecular electrostatic potential surface for E-TPDN (au).

(red, blue, and yellow)) in MEPS represent the regions of the most negative, positive, and slightly electron-rich region, respectively. In the present study, MEPS was calculated at the B3LYP/6–311++G(d, p) level. As illustrated in Fig. 9, the higher negative regions (ring 3 and OH) are the favored site for electrophilic attack and they are responsible for the attraction of protons by atomic nuclei corresponding to electrophilic reactivity [74]. So, for the blue zones, nucleophilic attacks are taking place, that is, these regions are responsible for the repulsion of a proton by atomic nuclei corresponding to nucleophilic reactivity [75].

4. Conclusion

In the present work, experimental (FTIR, UV–visible, 1H NMR, and 13C NMR), DFT, and TD-DFT calculations studies of E-TPDN were reported. B3LYP function with 6–311++*G*(d,p) basis set calculations of geometry optimization shown a perfect prediction of experimental geometric parameters. It was found that the theoretical vibrational frequencies, ^{1}H NMR, and ^{13}C NMR chemical shifts values are in good agreement with experimental values. Based on TD-DFT calculations and experimental UV-Vis spectral investigated in chloroform solvent, we were able to correlate the peak positions to the n-π^* and π-π^* electronic transition. The main peaks in UV-vis spectra are attributed to the HOMO-LUMO electronic transitions. The variation of some global reactivity descriptors of E-TPDN in three media has been investigated by the same model of calculation. This compound showed a much more chemical softer and high reactivity, in the gaseous phase, while it exhibits a good electrophile character in a polar solvent such as DMSO medium. The nonlinear optical property of E-TPDN was investigated by the determination of the ground-state dipole moment, the polarizability, first-, and second-order hyperpolarizabilities in the static and dynamic regimes using the DFT/CAM-B3LYP method. The obtained results show that this compound is considered a soft species as com-

pared to the unsubstituted form of this azo dye. Relatively low values of first-order hyperpolarizability are obtained due to the weak charge transfer in E-TPDN. The study showed that this azo dye has valuable second-statics and dyamics hyperpolarizabilities, and may have potential applications in the development of NLO materials. The Hirshfeld surface analysis and the subsequent 2D-fingerprint plots have indicated that the H…H, C…C, O…H/H…O, C…H/H…C, N…H/H…N and Br…H/H…Br contacts were the most significant contributors among the interacting atoms. 3D molecular surfaces were simulated in order to obtain information about possible sites for electrophilic and nucleophilic attacks. Thus the negative sites are on OH and ring 3 groups, whereas the positive potential sites are around the hydrogen atoms.

Declaration of Competing Interest

The authors declare that they have no known competing financial interests or personal relationships that could have appeared to influence the work reported in this paper.

Acknowledgments

The authors gratefully acknowledge the financial support via PRFU project from the Algerian Ministry of Higher Education and Scientific Research, the Directorate General of Scientific Research and Technological Development (DGRSDT), and Abdelhamid Ibn Badis University of Mostaganem.

References

[1] S. Benkhaya, A. El Harfi, S. El Harfi, Classifications, properties and applications of textile dyes: a review, Appl. J. Environ. Eng. Sci. 3 (2017) 311–320.
[2] A. Navarro, F. Sanz, Dye aggregation in solution: study of C.I. direct red I, Dyes Pigment. 40 (1999) 131–139.
[3] J.A. Mikroyannidis, D.V. Tsagkournos, S. Sharma, A. Kumar, Y.K. Vijay, G.D. Sharma, Efficient bulk heterojunction solar cells based on low band gap bisazo dyes containing anthracene and/or pyrrole units, Sol. Energy Mater. Sol. Cells 94 (2010) 2318–2327.
[4] H. Dinçalp, F. Toker, I. Durucasu, N. Avcibasi, S. Icli, New thiophene-based azo ligands containing azo methine group in the main chain for the determination of copper (II) ions, Dyes Pigment. 75 (2007) 11–24.
[5] M. Berradi, R. Hsissou, M. Khudhair, M. Assouag, O. Cherkaoui, A. El Bachiri, A. El Harfi, Textile finishing dyes and their impact on aquatic environs, Heliyon 5 (2019) e02711.
[6] A. Gürses, M. Açıkyıldız, K. Günes¸, M.S. Gürses, Classification of dye and pigments, in: Dyes and Pigments, Springer, 2016, pp. 31–45.
[7] R. Zhao, C. Tan, Y. Xie, C. Gao, H. Liu, Y. Jiang, One step synthesis of azo compounds from nitroaromatics and anilines, Tetrahedron Lett. 52 (2011) 3805–3809.
[8] G. Leriche, G. Budin, L. Brino, A. Wagner, Optimization of the azobenzene scaffold for reductive cleavage by dithionite; development of an azobenzene cleavable linker for proteomic applications, Eur. J. Org. Chem. 2010 (2010) 4360–4364.
[9] M. Fatima, R. Farooq, R.W. Lindström, M. Saeed, A review on biocatalytic decomposition of azo dyes and electrons recovery, J. Mol. Liq. 246 (2017) 275–281.
[10] R.G. Saratale, G.D. Saratale, D.C. Kalyani, I.S. Chang, S.P. Govindwar, Bacterial decolourisation and degradation of azo dyes - a review, J. Taiwan Inst. Chem. Eng. 42 (2011) 138–157.
[11] H. Lade, S. Govinwar, D. Paul, Mineralization and detoxification of the carcinogenic azo dye congo red and real textile effluent by a polyurethane foam immobilized microbial consortium in an up flow column bioreactor, Int. J. Environ. Res. Public Health 12 (2015) 6894–6918.
[12] B. Derkowska-Zielinska, L. Skowronski, T. Kozlowski, V. Smokal, A. Kysil, A. Biitseva, O. Krupka, Influence of peripheral substituents on the optical properties of heterocyclic azo dyes, Opt. Mater. 49 (2015) 325–329.
[13] E. Merino, M. Ribagorda, Control over molecular motion using the cis—trans photoisomerization of the azo group, Beilstein J. Org. Chem. 8 (2012) 1071–1090.
[14] B. Derkowska-Zielinska, L. Skowronski, A. Biitseva, A. Grabowski, M.K. Naparty, V. Smokal, A. Kysil, O. Krupka, Optical characterization of heterocyclic azo dyes containing polymers thin film, Appl. Surf. Sci. 421 (2017) 361–366.
[15] B.R. Kirthan, M.C. Prabhakara, H.S.B. Naik, P.H.A. Nayak, E.I. Naik, Synthesis, characterization, DNA interaction and anti-bacterial studies of Cu(ii), Co(ii) and Ni(ii) metal complexes containing azo-dye ligand, Chem. Data Collect. 29 (2020) 100506.
[16] A.M. Khedr, H. El-Ghamry, M.A. Kassem, F.A. Saad, N. El-Guesmi, Novel series of nanosized mono- and homobi-nuclear metal complexes of sulfathiazole azo dye ligand: synthesis, characterization, DNA-binding affinity, and anticancer activity, Inorg. Chem. Commun. 108 (2019) 107496.
[17] S. Benkhaya, O. Cherkaoui, M. Assouag, S. Mrabet, M. Rafik, A.E.L. Harfi, Synthesis of a new asymmetric composite membrane with bi-component collodion: application in the ultra-filtration of baths of reagent dyes of fabric rinsing/padding, J. Mater. Environ. Sci. 7 (2016) 4556–4569.
[18] L. Al-Rubaie, R.J. Mhessn, Synthesis and characterization of azo dye para red and new derivatives, J. Chem. 9 (2012) 465–470.
[19] L. Mansouri, B. Zouchoune, Substitution effects and electronic properties of the azo dye (1-phenylazo-2-naphthol) species: a TD-DFT electronic spectra investigation, Can. J. Chem. 93 (2014) 509–517.
[20] H. Benmansour, O. Boughzala, D. Dridi, D. Barillier, L. Chekir-Ghedira, R. Mosrati, Les colorants textiles sources de contamination de l'eau: criblage de la toxicité et des méthodes de traitement, J. Water Sci. 24 (2011) 209–238.
[21] P.T. Tasli, Ç.K. Atay, T. Demirturk, T. Tilki, Experimental and computational studies of newly synthesized azo dyes based materials, J. Mol. Struct. 1201 (2020) 127098.
[22] A.S. Abd-El-Aziz, A. Alsaggaf, E. Assirey, A. Naqvi, R.M. Okasha, T.H. Afifi, M. Hagar, A new family of benzo[h]chromene based azo dye: synthesis, *in-silico* and DFT studies with *in vitro* antimicrobial and antiproliferative assessment, Int. J. Mol. Sci. 22 (2021) 2807.
[23] A.K. Mohan, A. Purushothaman, D. Janardanan, K.R. Haridas, Experimental and theoretical studies of azo derivatives in terms of different donors, acceptors and position isomerism: synthesis, characterization and a combined electronic absorption, electrochemical and DFT study, J. Mol. Struct. 1249 (2022) 131621.
[24] M. Han, I. Abe, J. Oh, J. Jung, Y.J. Son, J. Noh, M. Hara, T. Seki, Solvent- and light-sensitive AIEE-active azo dye: from spherical to 1D and 2D assemblies, Int. J. Mol. Sci. 23 (2022) 965.
[25] R. Hsissou, F. Benhiba, S. Echihi, S. Benkhaya, M. Hilali, A. Berisha, S. Briche, A. Zarrouk, K. Nouneh, A. Elharfi, New epoxy composite polymers as a potential anticorrosive coating for carbon steel in 3.5% NaCl solution: experimental and computational approaches, Chem. Data Coll. 31 (2021) 100619.
[26] R. Hsissou, Review on epoxy polymers and its composites as a potential anticorrosive coating for carbon steel in 3.5% NaCl solution: computational approaches, J. Mol. Liq. 336 (2021) 116307.
[27] L. Kadiri, A. Ouass, R. Hsissou, Z. Safi, N. Wazzan, Y. Essaadaoui, I. Lebkiri, O. El Khattabi, E. Rifi, A. Lebkiri, Adsorption properties of coriander seeds: spectroscopic kinetic thermodynamic and computational approaches, J. Mol. Liq. 343 (2021) 116971.
[28] S. Bibi, M. Khan, S. ur-Rehman, M. Yaseen, S. Muhammad, R. Nadeem, N. Jahan, S. Noreen, Misbah, Investigation analysis of optoelectronic and structural properties of cis- and trans-structures of azo dyes: density functional theory study, J. Phys. Org. Chem. 34 (2021) e4183.
[29] N.N. Pesyan, V. Gholsanamloo, M.M. Par, H. Rashidnejad, A. Gharib, K. Nejati, Synthesis, characterization and spectroscopic properties of new azo dyes derived from aniline derivatives based on acetylacetone and azo-metal (II) complexes and singular value decomposition (SVD) investigation, Eurasian Chem. Commun. 7 (2019) 71–89.
[30] Z. Ngaini, H.B. Kui, Synthesis and antibacterial activity of azo and aspirin-azo derivatives, Malays. J. Anal. Sci. 21 (2017) 1183–1194.
[31] V.G. Nenajdenko, N.G. Shikhaliyev, A.M. Maharramov, K.N. Bagirova, G.T. Suleymanova, A.S. Novikov, V.N. Khrustalev, A.G. Tskhovrebov, Halogenated diazabutadiene dyes: synthesis, structures, supramolecular features, and theoretical studies, Molecules 25 (2020) 5013.
[32] S. Chetioui, I. Boudraa, S. Bouacida, A. Bouchoul, S. Bouaoud, (E)-1-[(2,4,6-Tribromophenyl)diazenyl]-naphthalen-2-ol, Acta Cryst. Struct. Rep. E69 (2013) o1250.
[33] M.J. Frisch, G.W. Trucks, H.B. Schlegel, G.E. Scuseria, M.A. Robb, J.R. Cheeseman, G. Scalmani, V. Barone, B. Mennucci, G.A. Petersson, H. Nakatsuji, M. Caricato, X. Li, H.P. Hratchian, A.F. Izmaylov, J. Bloino, G. Zheng, J.L. Sonnenberg, M. Hada, M. Ehara, K. Toyota, R. Fukuda, J. Hasegawa, M. Ishida, T. Nakajima, Y. Honda, O. Kitao, H. Nakai, T. Vreven, J.A. Montgomery, J.E. Peralta, F. Ogliaro, M. Bearpark, J.J. Heyd, E. Brothers, K.N. Kudin, V.N. Staroverov, R. Kobayashi, J. Normand, K. Raghavachari, A. Rendell, J.C. Burant, S.S. Iyengar, J. Tomasi, M. Cossi, N. Rega, J.M. Millam, M. Klene, J.E. Knox, J.B. Cross, V. Bakken, C. Adamo, J. Jaramillo, R. Gomperts, R.E. Stratmann, O. Yazyev, A.J. Austin, R. Cammi, C. Pomelli, J.W. Ochterski, R.L. Martin, K. Morokuma, V.G. Zakrzewski, G.A. Voth, P. Salvador, J.J. Dannenberg, S. Dapprich, A.D. Daniels, Ö. Farkas, J.B. Foresman, J.V. Ortiz, J. Cioslowski, D.J. Fox, Gaussian 09, Revision D.01, Gaussian Inc., Wallingford CT, 2009.
[34] E. Frisch, H.P. Hratchian, R.D. Dennington, T.A. Keith, John Millam, B. Nielsen, A.J. Holder, J. Hiscocks, Gaussian, Syntheses, Structural Elucidation, Thermal Properties, Theoretical Quantum Chemical Studies (DFT) and Biological Studies of Barbiturice Hydrazone Complexes Inc. GaussView version 5.0.8, 2009.
[35] N. Boukabcha, N. Benhalima, R. Rahmani, A. Chouaih, F. Hamzaoui, Theoretical investigation of electrostatic potential and nonlinear optical properties of meta–nitroacetanilide, Rasayan J. Chem. 8 (2015) 509–516.
[36] N. Boukabcha, A. Djafri, Y. Megrouss, O. Tamer, D. Avci, M. Tuna, N. Dege, A. Chouaih, Y. Atalay, A. Djafri, F. Hamzaoui, Synthesis, crystal structure, spectroscopic characterization and nonlinear optical properties of (Z)-N'-(2,4-dinitrobenzylidene)-2(quinolin-8-yloxy) acetohydrazide, J. Mol. Struct. 1194 (2019) 112–123.
[37] Ž.B. Milanović, D.S. Dimić, E.H. Avdović, D.A. Milenković, J.D. Marković, O.R. Klisurić, S.R. Trifunović, Z.S. Marković, Synthesis and comprehensive spec-

troscopic (X-ray, NMR, FTIR, UV-Vis), quantum chemical and molecular docking investigation of 3-acetyl-4 hydroxy 2-oxo-2H-chromen-7-yl acetate, J. Mol. Struct. 1225 (2021) 129256.
[38] Ž.B. Milanović, Z.S. Marković, D.S. Dimić, O.R. Klisurić, I.D. Radojević, D.S. Šeklić, M.N. Živanović, J.D. Marković, M. Radulović, E.H. Avdović, Synthesis, structural characterization, biological activity and molecular docking study of 4,7-dihydroxycoumarin modified by aminophenol derivatives, Comptes Rendus. Chim. 24 (2021) 215–232.
[39] J. Tomasi, B. Mennucci, R. Cammi, Quantum mechanical continuum solvation models, Chem. Rev. 105 (2005) 2999–3093.
[40] M.H. Jamroz, Vibrational Energy Distribution Analysis, VEDA 4, Warsaw, 2004.
[41] R. Dichfield, Self-consistent perturbation theory of diamagnetism, Mol. Phys. 27 (1974) 789–807.
[42] K. Wolinski, J.F. Hilton, P. Pulay, Efficient implementation of the gauge-independent atomic orbital method for NMR chemical shift calculations, J. Am. Chem. Soc. 112 (1990) 8251–8260.
[43] P. Agarwal, N. Choudhary, A. Gupta, P. Tandon, Density functional theory studies on the structure, spectra (FT-IR, FT-Raman, and UV) and first order molecular hyperpolarizability of 2-hydroxy-3-methoxy-N-(2-chloro-benzyl)-benzaldehyde-imine: comparison to experimental data, Vib. Spectrosc. 64 (2013) 134–147.
[44] A. Alparone, Second harmonic generation, electrooptical Pockels effect, and static first-order hyperpolarizabilities of 2,2'-Bithiophene conformers: an HF, MP2, and DFT theoretical investigation, Adv. Phys. Chem. 2013 (2013) 1–8.
[45] D.M. Bishop, I. Prigogine, S.A. Rice, molecular vibration and nonlinear optics, in: Advances in Chemical Physics, John Wiley & Soon, INC, New York, 1998, pp. 1–40.
[46] M.J. Turner, J.J. MacKinnon, S.K. Wolff, D.J. Grimwood, P.R. Spackman, D. Jayatilaka, M.A. Spackma, Crystal Explorer Ver. 17.5, University of Western Australia, 2017.
[47] K.S. Etsè, J. Dorosz, K.M. Christensen, J.Y. Thomas, L.B. Pop, E. Goffin, T. Colson, P. Lestage, L. Danober, B. Pirotte, J.S. Kastrup, P. Francotte, Development of thiochroman dioxide analogues of benzothiadiazine. Dioxides as new positive allosteric modulators of α-amino-3-hydroxy-5-methyl-4-isoxazolepropionic acid (AMPA) receptors, ACS Chem. Neurosci. 12 (2021) 2679–2692.
[48] P.R. Spackman, L.J. Yu, C.J. Morton, M.W. Parker, C.S. Bond, M.A. Spackman, D. Jayatilaka, S.P. Thomas, Bridging crystal engineering and drug discovery by utilizing intermolecular interactions and molecular shapes in crystals, Angew. Chem. Int. Ed. Engl. 58 (2019) 16780–16784.
[49] K.S. Etsè, A. Demonceau, G. Zaragoza, D. Serteyn, A. Mouithys-Mickalad, Design, synthesis and biochemical evaluation of novel 2-amino-3-(7-methoxybenzo[*d*][1,3]dioxol-5-yl)propanoic acid using horseradish peroxidase (HRP) activity, cellular ROS inhibition and molecular docking study, J. Mol. Struct. 1250 (2022) 131668.
[50] S.L. Tan, M.M. Jotanib, R.T. Edward, Utilizing Hirshfeld surface calculations, non-covalent interaction (NCI) plots and the calculation of interaction energies in the analysis of molecular packing, Acta Cryst. E75 (2019) 308–318.
[51] C.B. Pinto, L.H.R. Dos Santos, B.L. Rodrigues, Understanding metal–ligand interactions in coordination polymers using Hirshfeld surface analysis, Acta Cryst. C75 (2019) 707–716.
[52] N. Boukabcha, A. Direm, M. Drissi, Y. Megrouss, N. Khelloul, N. Dege, M. Tuna, A. Chouaih, Synthesis, structural determination, hirshfeld surface analysis, 3D energy frameworks, electronic and (static, dynamic) NLO properties of *o*-Nitroacetanilide (*o*-NAA): a combined experimental and quantum chemical study, Inorg. Chem. Commun. 133 (2021) 108884.
[53] K.S. Etsè, G. Zaragoza, K.D. Etsè, Easy preparation of novel 3,3-dimethyl-3,4-dihydro-2*H*-1,2,4-benzothiadiazine 1,1-dioxide: molecular structure, hirshfeld surface, NCI analyses and molecular docking on AMPA receptors, J. Mol. Struct. 1238 (2021) 130435.
[54] M.A. Spackman, J.J. McKinnon, Fingerprinting intermolecular interactions in molecular crystals, CrystEngComm 4 (2002) 378–392.
[55] J. Padmanabhan, R. Parthasarathi, M. Elango, V. Subramanian, B.S. Krishnamoorthy, S. Gutierrez-Oliva, A. Toro-Labbe, D.R. Roy, P.K. Chattaraj, Multiphilic descriptor for chemical reactivity and selectivity, J. Phys. Chem. A 111 (2007) 9130–9138.
[56] R. Parthasarathi, V. Subramanian, D.R. Royb, P.K. Chattaraj, Electrophilicity index as a possible descriptor of biological activity, Bioorg. Med. Chem. 12 (2004) 5533–5543.
[57] T. Koopmans, Über die zuordnung von wellenfunktionen und eigenwerten zu den einzelnen elektronen eines atoms, Physica 1 (1933) 104–113.
[58] R.S. Mulliken, A new electroaffinity scale; together with data on valence states and on valence ionization potentials and electron affinities, J. Chem. Phys. 2 (1934) 782–793.
[59] R.G. Parr, R.A. Donnelly, M. Levy, W.E. Palke, Electronegativity: the density functional viewpoint, J. Chem. Phys. 68 (1978) 3801–3807.
[60] R.G. Pearson, Hard and soft acids and bases, J. Am. Chem. Soc. 85 (1963) 3533–3539.
[61] R.G. Pearson, Hard and soft acids and bases, HSAB, part 1: fundamental principles, J. Chem. Educ. 45 (1968) 581–586.
[62] R.G. Pearson, Maximum chemical and physical hardness, J. Chem. Educ. 76 (1999) 267–275.
[63] R.G. Pearson, Absolute electronegativity and hardness correlated with molecular orbital theory, Proc. Nat. Acad. 83 (1986) 8440–8441.
[64] P.K. Chattaraj, D.R. Roy, Update 1 of: electrophilicity index, Chem. Rev. 107 (2007) 46–74.
[65] J. Aihara, Reduced HOMO-LUMO gap as an index of kinetic stability for polycyclic aromatic hydrocarbons, J. Phys. Chem. A 103 (1999) 7487–7495.
[66] K.S. Thanthiriwatte, K.M. Nalin de Silva, Non-linear optical properties of novel fluorenyl derivatives-*ab initio* quantum chemical calculations, J. Mol. Struct. Theochem. 617 (2002) 169–175.
[67] P.A. Limacher, K.V. Mikkelsen, H.P. Luthi, On the accurate calculation of polarizabilities and second hyperpolarizabilities of polyacetylene oligomer chains using the CAM-B3LYP density functional, J. Chem. Phys. 130 (2009) 194114.
[68] M. Medved, Š. Budzák, T. Pluta, Static NLO responses of fluorinated polyacetylene chains evaluated with long-range corrected density functionals, Chem. Phys. Lett. 515 (2011) 78–84.
[69] A. Alparone, Response electric properties of α-helix polyglycines: a CAM-B3LYP/DFT investigation, Chem. Phys. Lett. 563 (2013) 88–92.
[70] M. Torrent-Sucarrat, M. Sola, M. Duran, J.M. Luis, B. Kirtman, Basis set and electron correlation effects on *ab initio* electronic and vibrational nonlinear optical properties of conjugated organic molecules, J. Chem. Phys. 118 (2003) 711–718.
[71] J. Zyss, Octupolar organic systems in quadratic nonlinear optics: molecules and materials, Nonlinear Opt. 1 (1991) 3–18.
[72] A. Eşme, S.G. Sağdinç, The linear, nonlinear optical properties and quantum chemical parameters of some Sudan dyes, BAÜ Fen Bil. Enst. Dergisi. Cilt. 16 (2014) 47–75.
[73] E. Scrocco, J. Tomasi, Electronic molecular structure, reactivity and intermolecular forces: a euristic interpretation by means of electrostatic molecular potentials, Adv. Quantum Chem. 11 (1978) 116–193.
[74] F.J. Luque, J.M. López, M. Orozco, Perspective on electrostatic interactions of a solute with a continuum. A direct utilization of Ab-initio molecular potentials for the prevision of solvent effects, Theor. Chem. Acc. 103 (2000) 343–345.
[75] M. Bourass, A. Touimi Benjelloun, M. Benzakour, M. Mcharfi, F. Jhilal, F. Serein-Spirau, J. Marc Sotiropoulos, M. Bouachrine, DFT/TD-DFT characterization of conjugational electronic structures and spectral properties of materials based on thieno[3,2-*b*][1]benzothiophene for organic photovoltaic and solar cell applications, J. Saudi Chem. Soc. 21 (2017) 563–574.